Spin-Polarization Control of Photoelectrons Using Poincaré Fields

Daniel Younis,[1,*] Daniel F. Gordon,[2] and Bahman Hafizi[2]
[1]*Department of Physics and Astronomy, University of Rochester, Rochester, New York 14627, USA*
[2]*Naval Research Laboratory, Washington, DC 20375, USA*

(Received 6 February 2024; revised 28 May 2024; accepted 18 June 2024; published 22 July 2024)

Efficient helicity transfer from Poincaré fields to electrons of hydrogenic ions is revealed for the first time by four-dimensional relativistic simulations. The magnetic multipole class of Poincaré fields is chosen due to its fundamental role in light-matter spin coupling, and the calculation is demonstrated for Ne^{9+} ion irradiated by single and multimode x-ray pulses. Photoelectrons of both helicities emerge synchronously from the ion ensemble, and their directionality is controllable through the radiation mode numbers. The helicity density distributions display novel structures composed of jets, spirals, and rings, among others, that are unique to the combination of atomic and field parameters. Our approach to generate spin-polarized leptons using Poincaré fields may provide a new platform for helicity characterization based on advanced numerical capabilities.

DOI: 10.1103/PhysRevLett.133.043201

Introduction—Spin-polarized leptons are essential for precision tests of the standard model of particle physics, and in going beyond to search for new particles, interactions, and symmetries [1,2]. For example, in experimental searches of the smuon particle [3], the use of colliding $e^{\pm}$ beams that are oppositely polarized is critical to suppress background $W^{\pm}$ boson production [1]. With the advent of multipetawatt laser technology, experimental studies of ultra-high-intensity light-matter interaction and nonlinear QED are also rapidly becoming available [4–10]. A variety of QED processes involve the transfer of orbital and spin angular momentum, such as the Bethe-Heitler process with circularly polarized photons [11–13], nuclear [11,14] and magnetic bremsstrahlung radiation [15], Coulomb scattering of leptons [16], and photoionization with Bessel beams [17,18], Laguerre-Gauss modes [19–21], and circularly polarized laser fields [9,14,22–25] (see also Ref. [26], wherein linear polarization is treated in laser-ion spin coupling).

In this Letter, we consider spin-resolved photoionization due to light that is spatially structured in all respects—intensity, phase, polarization, and orbital angular momentum. This is the first semiclassical photoionization theory (to the best of our knowledge) that considers fully structured light without any paraxial approximation. The field states are classified as fully structured, or full-Poincaré fields, as the union of Stokes vectors from each spatial point covers every polarization state on the Poincaré sphere [27–30]. A common construction of a Poincaré field is a superposition of orthogonally polarized Laguerre-Gauss modes, generally with a relative phase [27,31]. However, in the case of light-matter spin coupling, a more natural choice of basis is the electromagnetic multipole modes [32–34] because they are simultaneous eigenfunctions of the total angular momentum operator $\hat{\jmath}$ and its projection $\hat{\jmath}_z$.

Poincaré fields of the magnetic multipole type can synchronously produce photoelectrons of both helicities, in contrast to the fixed helicities produced by plane, circularly polarized waves [14,22–25] (see Ref. [35] for a review). This is because in the near field of a Poincaré field where a paraxial representation is not possible, an atom experiences a complex distribution of polarization states and angular momentum densities that define the mode. (One may find it useful to regard this scenario as the inverse of a typical atomic radiation problem, wherein the multipole modes are converging toward the atom, instead of being radiated away from it.) Consequently, the Poincaré field determines the angular distribution of photoelectron helicity, which for a given direction can assume an expectation value anywhere between $\pm\hbar/2$. A recent investigation [34] considered only the first-order S-matrix element describing one-photon ionization, which is the practical limit because a Volkov state solution [36,37] for leptons dressed by a Poincaré field does not exist. Thus, a complete numerical integration is now necessary to advance.

In this Letter, we present the first results of a Dirac electron irradiated by a semiclassical Poincaré field. We accomplish this through state-of-the-art *ab initio* simulations in full $(3+1)$ dimensionality that enable the field-dressed state to be incorporated. As a result, the calculation goes beyond few-order S-matrix theory and into the realm of empirical study. No approximations are made beyond the discretization of spacetime and use of a soft-core atomic potential [38,39]. However, the computational expense of modeling the relativistic interaction [40] means that the viable parameter space is presently limited to high-frequency, few-cycle pulses.

*Contact author: dan.younis@outlook.com

We consider the high-intensity tunneling ionization regime characterized by the Keldysh parameter $\Upsilon = \sqrt{2I_p/a_0^2 m_e} \ll 1$ [41,42], where $I_p/m_e = 1 - \sqrt{1-(Z\alpha)^2}$ is the ionization potential and $a_0 = |e|E_0/\omega m_e$ is the normalized field amplitude. Note that a_0 also gives the energy absorbed by a free electron over one Compton wavelength $\lambdabar_c = m_e^{-1} \approx 3.86 \times 10^{-11}$ cm in units of the field frequency ω, and that $a_0 \gg 1$ results in ultrarelativistic free-electron motion. Here, $e < 0$ and m_e are the electron charge and mass, Z is the nuclear charge, and α is the fine-structure constant. Natural units are used ($\hbar = c = 1$) except where otherwise indicated.

We present calculations of the momentum-space helicity distribution for hydrogenic neon ion Ne^{9+} ($I_p/m_e \approx 2.67 \times 10^{-3}$) irradiated by single and multimode Poincaré fields of the magnetic multipole type, having amplitude $a_0 = 10$ ($I_0 \approx 1.14 \times 10^{29}$ W/cm^2) and frequency $\omega = 0.07 m_e \approx 36$ keV ($\lambda \approx 0.0347$ nm, x-ray). In this case, the Keldysh parameter $\Upsilon \approx 7.3 \times 10^{-3}$ is well within the regime of tunneling ionization.

A semiclassical description of the field is justified by the value of a_0, which implies a large photon number of $\mathcal{O}(10^7)$ per λ^3 volume. The intensity and wavelength are chosen to induce a non-negligible degree of ionization. The intensity considered here is approximately half of the Schwinger value. The wavelength should be comparable to the characteristic atomic length, because the spherical multipole modes create an intensity null at the point of convergence that will inhibit ionization if $\lambda \gg \lambdabar_c$. We note that the wavelength employed here is slightly shorter than that producible by modern-day free-electron lasers (e.g., the European XFEL [43]).

For illustration, Fig. 1 shows the Ne^{9+} electron charge density before and after irradiation by a 2-cycle magnetic quadrupole field. The first panel corresponds to time zero, when the field is converging toward the nucleus, and the second panel is postinteraction when the field is diverging

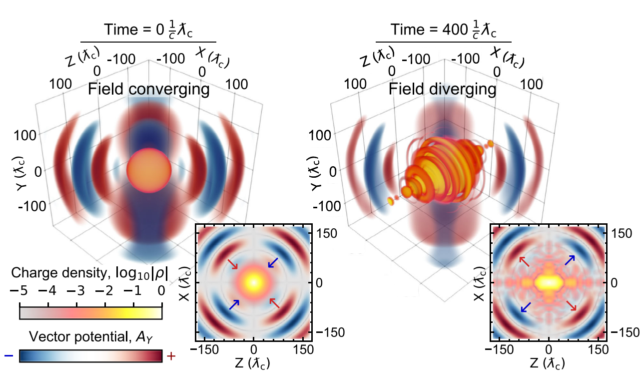

FIG. 1. Snapshots of a magnetic quadrupole $(j, m) = (2, 0)$ Poincaré field irradiating Ne^{9+} ion. Orange color map: charge density $\log_{10}|\rho|$. Red-blue color map: vector potential component $A_y(\mathbf{r}, t)$. Subpanels: cross-sectional views for $y = 0$.

and the photoelectron waves are scattering out. The objective lies in analyzing the helicity content of the ionized wave packets to understand how different Poincaré field modes imprint their spin angular momentum characteristics.

Atomic and field potentials—The starting point of the calculation is the time-dependent Dirac equation,

$$[\gamma_\mu(\hat{p}^\mu + |e|A^\mu) - m_e]|\psi\rangle = 0. \qquad (1)$$

It is numerically integrated using an explicit finite-difference scheme implemented in the TURBOWAVE code, the details of which can be found in Refs. [44–46]. Here, $|\psi\rangle$ is the bispinor wave function, γ_μ are the Dirac matrices in standard representation, $\hat{p}^\mu = i\partial^\mu$ is the four-momentum operator, and $A^\mu = (A^0, \mathbf{A})$ is the four-potential.

The system consists of a hydrogenic ion, i.e., an atom for which all but the innermost electron have been predetached. It is modeled by a softened Coulombic potential of the form $A^0(\mathbf{r}) = -Z\alpha/\sqrt{|\mathbf{r}|^2 + \delta r^2}$, where δr is the screening radius [39]. A nonzero value for δr removes the $1/r$ singularity, and it also determines the model eigenenergy spectrum and ionization potential. In three dimensions, the energy levels approach the exact atomic values as $\delta r \to 0$ [47]. Thus, δr should be chosen numerically small but still greater than the spatial resolution, which itself must be less than the Compton wavelength. In all cases, the wave function is initialized in the electron spin-up ground state (total angular momentum $j = \ell + m_s = 1/2$).

The incident radiation field is spherical in nature, belonging to the magnetic multipole class of Poincaré fields. The vector potential is initialized in the far field with Fourier components [32,33]

$$\mathbf{A}_{jm}(\mathbf{k}, t) = \Re A_0 \mathbf{\Phi}_{jm}(\vartheta_{\hat{\mathbf{k}}}, \varphi_{\hat{\mathbf{k}}})\delta(|\mathbf{k}| - \omega)e^{-i\omega t} \qquad (2)$$

and the TURBOWAVE electromagnetic field solver computes the near-field potential automatically. In Eq. (2), $\Re$ denotes the real component of the entire quantity, $\hat{\mathbf{k}} = \mathbf{k}/\omega$ is the unit wave vector, $\mathbf{\Phi}_{jm}(\vartheta_{\hat{\mathbf{k}}}, \varphi_{\hat{\mathbf{k}}}) = \hat{\mathbf{k}} \times \mathbf{\nabla}_{\hat{\mathbf{k}}} Y_{jm}(\vartheta_{\hat{\mathbf{k}}}, \varphi_{\hat{\mathbf{k}}})$ are vector spherical harmonic functions, and (j, m) enumerate the total and projected angular momentum mode numbers, $j \geq 1$ and $|m| < j - 1$. Exact functional forms of $\mathbf{A}_{jm}(\mathbf{r}, t)$ are provided in the Supplemental Material [48]. In the calculation results that follow, the vector potential is modulated by a Gaussian-like polynomial to produce a two-cycle pulse. We will consider situations in which the field converges symmetrically upon the atom, as depicted in Fig. 1, in addition to the case of imperfect (off-center) focusing, which is more realistic from an experimental standpoint.

Calculation of helicity—Following interaction with the field, the wave function separates spatially into bound and free (photoionized) components, $|\psi\rangle = |\psi_b\rangle + |\tilde{\psi}\rangle$. In practice, the bound part $\langle \mathbf{r}|\psi_b\rangle$ is filtered by applying to

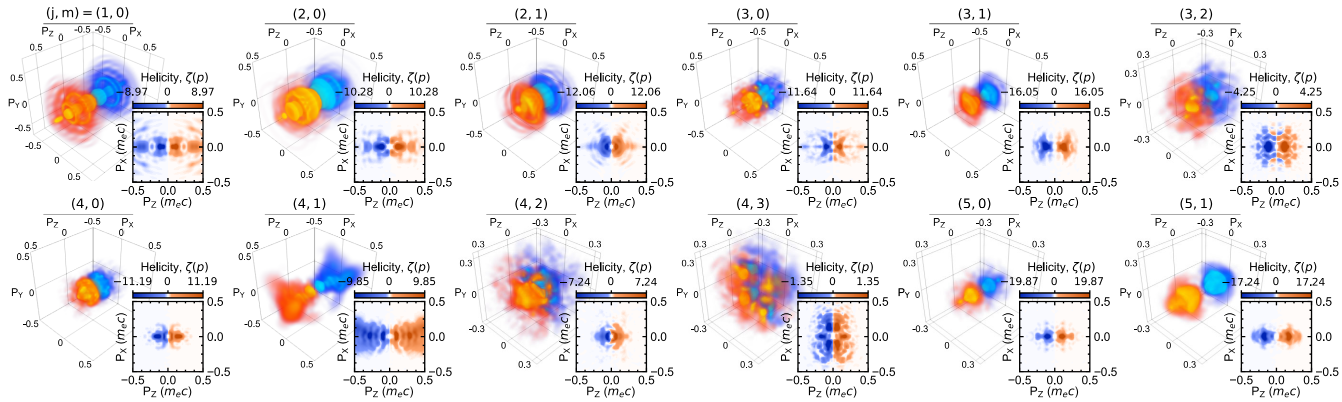

FIG. 2. Single-mode ionization case. Helicity density distributions $\zeta(\mathbf{p})$ of hydrogenic neon ion Ne^{9+} following irradiation by magnetic multipole fields of mode numbers $(j, m \geq 0)$ as labeled. Orange (blue) represents a positive (negative) helicity expectation value. Subpanels: cross-sectional views for $p_y = 0$.

each of the bispinor components a masking function of the form $\mathcal{M}_\mu(\mathbf{r}) = 1 - \exp(-|\mathbf{r}|^4/\mu^4)$, $\mu = 20\lambda\!\!\!^{-}_c$. The wave function is subsequently Fourier-transformed $\langle \mathbf{r}|\tilde{\psi}\rangle \to \langle \mathbf{p}|\tilde{\psi}\rangle \equiv \tilde{\psi}(\mathbf{p})$ and a momentum-space filter $\mathcal{M}_\mu(\mathbf{p})$ with $\mu = 0.05 m_e c$ is applied to mask low-energy photoelectrons from view [48]. The helicity density is given by the expectation value

$$\zeta(\mathbf{p}) = \langle \tilde{\psi}(\mathbf{p})|\left(\mathbf{n} \cdot \tfrac{1}{2}\mathbf{\Sigma}\right)|\tilde{\psi}(\mathbf{p})\rangle, \tag{3}$$

wherein the inner product is over bispinor components, $\mathbf{n} \equiv \mathbf{p}/|\mathbf{p}|$ is the momentum direction, and $\mathbf{\Sigma} = \boldsymbol{\sigma}\hat{\mathbb{1}}$ with $\boldsymbol{\sigma}$ the Pauli matrices. In evaluating $\zeta(\mathbf{p})$, it is important that the wave function and field components have negligible spatial overlap in order that $|\tilde{\psi}\rangle$ obeys a quasifree Hamiltonian wherein $\mathbf{p}$ is the kinetic momentum. Note that the plane-wave helicity eigenstates satisfy $\int d^3p\,\zeta(\mathbf{p}) = \pm 1/2$ (Supplemental Material) [33].

Single-mode ionization—We present in Fig. 2 the momentum-helicity distribution $\zeta(\mathbf{p})$ for 12 individual cases, corresponding to irradiation by single-mode magnetic multipoles with $(j, m \geq 0)$ up to the (5, 1) mode, as labeled. These distributions are produced at the final simulation time step, at which point the field has outrun the wave function. The panel for $(j, m) = (2, 0)$ (quadrupole mode) corresponds to the simulation time sequence presented in Fig. 1.

A number of interesting features appear in the helicity distributions. Photoelectrons with momenta $p_z > 0$ predominantly carry helicities $\zeta(\mathbf{p}) > 0$, and vice versa for $p_z, \zeta(\mathbf{p}) < 0$. However, in some cases the p_z hemispheres contain a mixture of positive and negative helicity expectation values, as in the (3, 2) and (4, 3) mode cases. In addition, the helicity sign along the p_z poles is that of the corresponding hemisphere. Moreover, we observe that irradiation by single-mode photons can produce nonazimuthally symmetric helicity distributions. This appears most prominently in the jetlike structures in the (4, 1) and (4, 3) mode cases of Fig. 2, or the helicity spirals in the (2, 1) and (3, 2) cases. These more intricate, off-p_z-axis features in the helicity density, which are of comparatively smaller magnitude, may be contained in the higher-order S-matrix terms that are difficult to calculate without a Poincaré-Volkov state solution of the Dirac equation.

The momentum-helicity distributions also display a variety of symmetries worth noting. In all cases, the integrated value $\int d^3p\,\zeta(\mathbf{p})$ is negligible, indicating nearly equal production of positive and negative helicity photoelectrons. Additionally, if the Dirac bispinor is initialized in the e^- spin-down state, the $\zeta(\mathbf{p})$ of Fig. 2 will appear π-rotated through the p_y axis. For irradiation by modes with $m < 0$, the features are similarly mirrored. In particular, the $(2, -1)$, $(3, -1)$, and $(5, -1)$ modes produce helicity spirals that are rotating in the opposite sense as their $m > 0$ counterparts. In the Supplemental Material, the $m < 0$ mode distributions are provided.

Multimode ionization—Consider a field that is an even superposition of two multipole modes $(j_1, m_1) + (j_2, m_2)$ with all other parameters unchanged. Figure 3 shows the photoelectron helicity distribution $\zeta(\mathbf{p})$ due to various multimode field combinations. In this case, a key distinction that arises is a nonvanishing net polarization, $\int d^3p\,\zeta(\mathbf{p}) \neq 0$. For instance, in the $(j, m) = (1, 0) + (2, 0)$ panel, we observe a large, negative helicity-density value for momenta $p_z < 0$. Based on the mode numbers alone, it is not intuitive why this jetlike structure should appear. One must instead analyze how interference between the modes of the composite field results in asymmetrical illumination of the Ne^{9+} wave function. The $(1, 0) + (2, 0)$ mode superposition, in particular, ejects a dense wave packet traveling in the $-z$ direction, endowed mostly with negative helicity.

Similar relativistic helicity jets appear in the $(4, 1) + (4, 2)$ and $(3, -1) + (4, -1)$ mode cases. In the $p_y = 0$ plane of the $(3, -2) + (4, -2)$ case, there is a trident-shaped distribution formed by one negative-helicity jet that

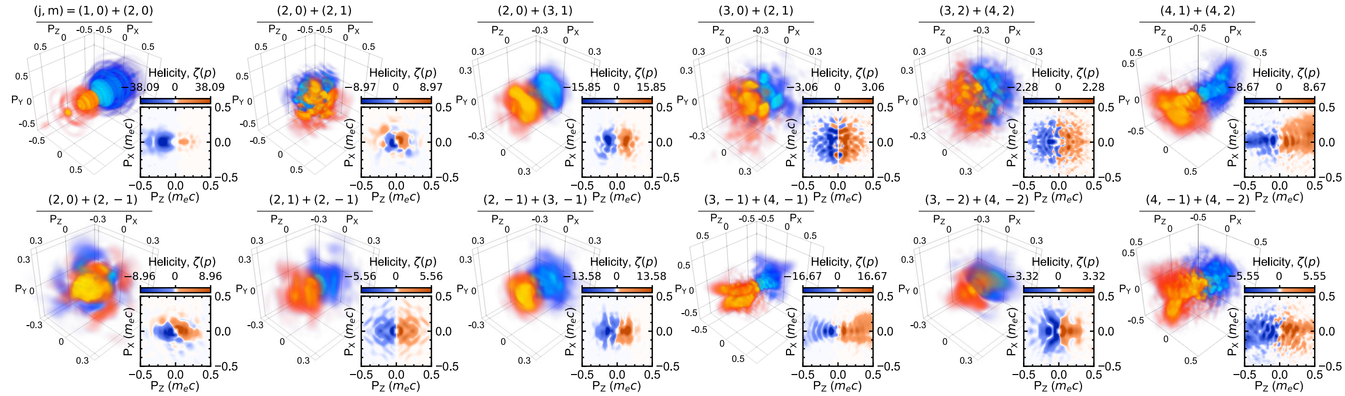

FIG. 3. Multimode ionization case. Helicity density distributions $\zeta(\mathbf{p})$ of hydrogenic neon ion Ne^{9+} following irradiation by superpositions of magnetic multipole fields with mode numbers $(j_1, m_1) + (j_2, m_2)$ as labeled. Orange (blue) represents a positive (negative) helicity expectation value. Subpanels: cross-sectional views for $p_y = 0$. The top row consists solely of m_1, $m_2 \geq 0$ modes, whereas the bottom row has some m_1, $m_2 < 0$ modes.

is parallel to the p_x axis, and two that are along the $p_x = \pm p_z$ diagonals. Some combinations produce complex distributions with little regularity and high asymmetry, as with the $(3,2) + (4,2)$ and $(4,-1) + (4,-2)$ superpositions.

Evidently, each combination of modes has a unique photoelectron helicity signature. This suggests that a measurement of the helicity density may serve as a method of characterizing the angular momentum content of a given radiation field. A more exhaustive search in parameter space would be needed to understand the field conditions that produce specific structures in the helicity distribution.

Effect of focal-point misalignment—Experimentally, it would be difficult to align an atom with wavelength-scale precision in order that a spherical Poincaré wave converges upon it with perfect symmetry. Nevertheless, if the focal point is slightly misaligned with the ion, photoelectrons with structured polarization attributes may still be produced. Returning to the $(j, m) = (1, 0)$ (dipole) mode case, the calculation is repeated with the field now focusing to the point $\mathbf{r}_f = (0, 0, -10)\lambda\!\!\!^{-}_c$ and the Ne^{9+} ionic potential centered at the origin as before [51].

In the first three panels of Fig. 4, snapshots of the simulation time sequence are shown. Here, around the time that the field has reached its focus ($t \approx 200\lambda\!\!\!^{-}_c/c$, Panel 2), we observe a "pinching" of the charge density that releases a higher density photoelectron wave traveling in the forward ($+z$) direction than in the backward ($-z$) direction. The resultant helicity distribution (Panel 4) displays similar relativistic jet and ring structures as before (compare to the (1,0) mode centered-focus case of Fig. 2), but now the positive helicity signal for $p_z > 0$ has been enhanced (and conversely, the negative helicity signal has been suppressed), and there is a net positive integrated value. Note the $\zeta(\mathbf{p})$ distribution of the (1, 0) mode in Fig. 2 attains a maximum value of $|\zeta|_{\max} \approx 19.35$, whereas in this case it is $|\zeta|_{\max} \approx 64.28$.

In practice, it may be possible to exploit misalignment in the focus to obtain relative control over the directionality, structure, and degree of photoelectron polarization.

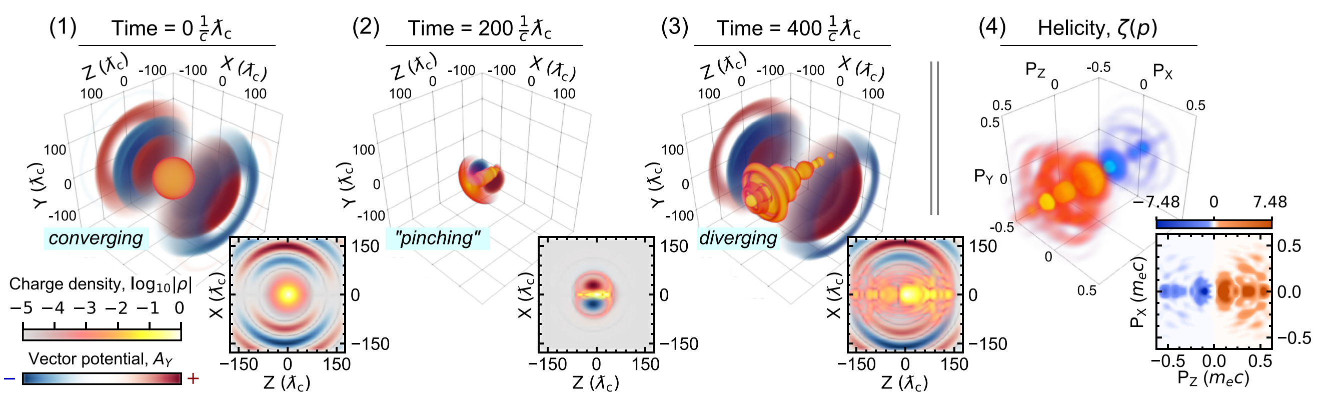

FIG. 4. Illustration of the effect of focal-point misalignment with the ion. Panels (1)–(3): snapshots in time of an offset magnetic dipole field $(j, m) = (1, 0)$ irradiating Ne^{9+} ion. Panel (4): the resultant helicity density distribution (compare with that of Fig. 2). Sub-panels: cross-sectional views for y, $p_y = 0$.

An alignment tolerance at the Compton scale still presents challenges. For this scenario to be practical, it may be necessary to consider novel targets that behave like an atom yet are much larger [52,53].

Summary and outlook—The complex distribution of polarization states and angular momentum densities that define a Poincaré field state can be utilized, through photoionization, to produce structured electron helicity distributions of both positive and negative expectation values. This has been demonstrated numerically using an *ab initio* approach based on the time-dependent Dirac equation, specifically for the Ne^{9+} hydrogenic ion irradiated by single and multimode x-ray Poincaré fields. The numerical approach supersedes what is possible through S-matrix calculations, which are severely limited without an analytic solution to the Dirac equation describing a Poincaré-dressed Volkov state. In contrast, an *ab initio* numerical approach facilitates a more realistic semiclassical treatment in the tunneling ionization regime, and so provides a new avenue for characterization and control of photoelectron helicity.

Acknowledgments—This research has benefited from insightful discussions with J. H. Eberly, A. Di Piazza, S.-X. Hu, and P. Milonni, whom we thank. This work was supported by NRL 6.1 Base Funds and by the U.S. DOE Office of Science under Interagency Agreement No. 89243018SSC000006. Calculations were performed on the NERSC-Perlmutter supercomputing cluster.

[1] G. Moortgat-Pick, T. Abe, G. Alexander, B. Ananthanarayan, A. A. Babich, V. Bharadwaj, D. Barber, A. Bartl, A. Brachmann, S. Chen *et al.*, Polarized positrons and electrons at the linear collider, Phys. Rep. **460**, 131 (2008).

[2] T. Okugi, Y. Kurihara, M. Chiba, A. Endo, R. Hamatsu, T. Hirose, T. Kumita, T. Omori, Y. Takeuchi, and M. Yoshioka, Proposed method to produce a highly polarized e^+ beam for future linear colliders, Jpn. J. Appl. Phys. **35**, 3677 (1996).

[3] The smuon is the hypothesized supersymmetric counterpart to the muon.

[4] G. A. Mourou, T. Tajima, and S. V. Bulanov, Optics in the relativistic regime, Rev. Mod. Phys. **78**, 309 (2006).

[5] A. Di Piazza, C. Müller, K. Z. Hatsagortsyan, and C. H. Keitel, Extremely high-intensity laser interactions with fundamental quantum systems, Rev. Mod. Phys. **84**, 1177 (2012).

[6] A. Di Piazza and A. I. Milstein, Quasiclassical approach to high-energy QED processes in strong laser and atomic fields, Phys. Lett. B **717**, 224 (2012).

[7] T. Nakamura, J. K. Koga, T. Zh. Esirkepov, M. Kando, G. Korn, and S. V. Bulanov, High-power γ-ray flash generation in ultraintense laser-plasma interactions, Phys. Rev. Lett. **108**, 195001 (2012).

[8] S. Weber *et al.*, P3: An installation for high-energy density plasma physics and ultra-high intensity laser–matter interaction at ELI-Beamlines, Matter Radiat. Extremes **2**, 149 (2017).

[9] A. Di Piazza, A. I. Milstein, and C. Müller, Polarization of the electron and positron produced in combined Coulomb and strong laser fields, Phys. Rev. A **82**, 062110 (2010).

[10] D. Younis, B. Hafizi, and D. F. Gordon, Generation of collimated vortex gamma-rays from intense Poincaré beam–plasma interaction, Phys. Plasmas **29**, 093106 (2022).

[11] H. Olsen and L. C. Maximon, Photon and electron polarization in high-energy bremsstrahlung and pair production with screening, Phys. Rev. **114**, 887 (1959).

[12] C. Müller, Nonlinear Bethe–Heitler pair creation with attosecond laser pulses at the LHC, Phys. Lett. B **672**, 56 (2009).

[13] T.-O. Müller and C. Müller, Spin correlations in nonperturbative electron–positron pair creation by petawatt laser pulses colliding with a TeV proton beam, Phys. Lett. B **696**, 201 (2011); Longitudinal spin polarization in multiphoton Bethe-Heitler pair production, Phys. Rev. A **86**, 022109 (2012).

[14] R. H. Pratt, R. A. Müller, and A. Surzhykov, Sum rules for the polarization correlations in photoionization and bremsstrahlung, Phys. Rev. A **93**, 053421 (2016).

[15] A. A. Sokolov and I. M. Ternov, *Radiation from Relativistic Electrons* (American Institute of Physics, New York, NY, 1986).

[16] R. H. Pratt, Transfer of helicity in radiation and absorption of high-energy photons, Phys. Rev. **123**, 1508 (1961).

[17] O. Matula, A. G. Hayrapetyan, V. G. Serbo, A. Surzhykov, and S. Fritzsche, Atomic ionization of hydrogen-like ions by twisted photons: angular distribution of emitted electrons, J. Phys. B **46**, 205002 (2013).

[18] A. Surzhykov, D. Seipt, V. G. Serbo, and S. Fritzsche, Interaction of twisted light with many-electron atoms and ions, Phys. Rev. A **91**, 013403 (2015).

[19] A. Picón, J. Mompart, J. R. Vázquez de Aldana, L. Plaja, G. F. Calvo, and L. Roso, Photoionization with orbital angular momentum beams, Opt. Express **18**, 3660 (2010).

[20] A. Picón, A. Benseny, J. Mompart, J. R. Vázquez de Aldana, L. Plaja, G. F. Calvo, and L. Roso, Transferring orbital and spin angular momenta of light to atoms, New J. Phys. **12**, 083053 (2010).

[21] T. P. Simula, N. Nygaard, S. X. Hu, L. A. Collins, B. I. Schneider, and K. Mølmer, Angular momentum exchange between coherent light and matter fields, Phys. Rev. A **77**, 015401 (2008).

[22] U. Fano, Spin orientation of photoelectrons ejected by circularly polarized light, Phys. Rev. **178**, 131 (1969).

[23] I. Barth and O. Smirnova, Spin-polarized electrons produced by strong-field ionization, Phys. Rev. A **88**, 013401 (2013).

[24] D. Trabert, A. Hartung, S. Eckart, F. Trinter, A. Kalinin, M. Schöffler, L. Ph. H. Schmidt, T. Jahnke, M. Kunitski, and R. Dörner, Spin and angular momentum in strong-field ionization, Phys. Rev. Lett. **120**, 043202 (2018).

[25] M.-M. Liu, Y. Shao, M. Han, P. Ge, Y. Deng, C. Wu, Q. Gong, and Y. Liu, Energy- and momentum-resolved photoelectron spin polarization in multiphoton ionization of Xe by circularly polarized fields, Phys. Rev. Lett. **120**, 043201 (2018).

[26] S. X. Hu and C. H. Keitel, Spin signatures in intense laser-ion interaction, Phys. Rev. Lett. **83**, 4709 (1999).
[27] A. M. Beckley, T. G. Brown, and M. A. Alonso, Full Poincaré beams, Opt. Express **18**, 10777 (2010); Full Poincaré beams II: Partial polarization, Opt. Express **20**, 9357 (2012).
[28] G. Milione, H. I. Sztul, D. A. Nolan, and R. R. Alfano, Higher-order Poincaré sphere, Stokes parameters, and the angular momentum of light, Phys. Rev. Lett. **107**, 053601 (2011).
[29] D. Naidoo, F. S. Roux, A. Dudley, I. Litvin, B. Piccirillo, L. Marrucci, and A. Forbes, Controlled generation of higher-order Poincaré sphere beams from a laser, Nat. Photonics **10**, 327 (2016).
[30] A. Forbes, M. de Oliveira, and M. R. Dennis, Structured light, Nat. Photonics **15**, 253 (2021).
[31] J. Morgan, E. Hemsing, B. W. J. McNeil, and A. Yao, Free electron laser generation of x-ray Poincaré beams, New J. Phys. **22**, 072001 (2020).
[32] J. D. Jackson, *Classical Electrodynamics*, 2nd ed. (Wiley, New York, US, 1975).
[33] V. B. Berestetskiĭ, E. M. Lifshitz, and L. P. Pitaevskiĭ, *Quantum Electrodynamics*, 2nd ed. (Butterworth-Heinemann, Oxford, UK, 2008).
[34] B. Hafizi, D. Younis, and D. F. Gordon, Polarized photoelectrons from converging vector waves, New J. Phys. **24**, 103029 (2022).
[35] N. A. Cherepkov, *Spin Polarization of Atomic and Molecular Photoelectrons* (Academic Press, New York, 1983), pp. 395–447.
[36] D. M. Wolkow, On a class of solutions of the Dirac equation, Z. Phys. **94**, 250 (1935).
[37] M. Klaiber, E. Yakaboylu, and K. Z. Hatsagortsyan, Above-threshold ionization with highly charged ions in superstrong laser fields. I. Coulomb-corrected strong-field approximation, Phys. Rev. A **87**, 023417 (2013); Above-threshold ionization with highly charged ions in superstrong laser fields. II. Relativistic Coulomb-corrected strong-field approximation, Phys. Rev. A **87**, 023418 (2013).
[38] J. Javanainen, J. H. Eberly, and Q. Su, Numerical simulations of multiphoton ionization and above-threshold electron spectra, Phys. Rev. A **38**, 3430 (1988).
[39] Q. Su and J. H. Eberly, Model atom for multiphoton physics, Phys. Rev. A **44**, 5997 (1991).
[40] B. Hafizi, D. F. Gordon, and J. P. Palastro, First benchmark of relativistic photoionization theories against 3D *ab initio* simulation, Phys. Rev. Lett. **118**, 133201 (2017).
[41] L. V. Keldysh, Ionization in the field of a strong electromagnetic wave, J. Exp. Theor. Phys. **20**, 1307 (1965), https://inspirehep.net/literature/1793133.
[42] S. V. Popruzhenko, Keldysh theory of strong field ionization: history, applications, difficulties and perspectives, J. Phys. B **47**, 204001 (2014).
[43] W. Decking *et al.*, A MHz-repetition-rate hard X-ray free-electron laser driven by a superconducting linear accelerator, Nat. Photonics **14**, 391 (2020).
[44] D. F. Gordon, B. Hafizi, and M. H. Helle, Solution of relativistic quantum optics problems using clusters of graphical processing units, J. Comput. Phys. **267**, 50 (2014).
[45] D. F. Gordon and B. Hafizi, Relativistic photoionization calculations with the time dependent Dirac equation, Technical Report, Naval Research Laboratory, 2016, NRL/MR/6795–16-9698.
[46] D. F. Gordon, turboWAVE v4.8.0, https://github.com/USNavalResearchLaboratory/turboWAVE (2023).
[47] C. Li, Exact analytical solution of the ground-state hydrogenic problem with soft Coulomb potential, J. Phys. Chem. A **125**, 5146 (2021).
[48] See Supplemental Material, which includes Refs. [49,50], at http://link.aps.org/supplemental/10.1103/PhysRevLett.133.043201 for the degree of ionization and masked population data.
[49] *Handbook of Mathematical Functions*, edited by M. Abramowitz and I. A. Stegun (Dover, New York, 1965).
[50] J. A. Nelder and R. Mead, A simplex method for function minimization, Comput. J. (UK) **7**, 308 (1965).
[51] The degree of misalignment is approximately 10× the ionic radius, $r_{\mathrm{ion}} \sim 1/Z$.
[52] M. Amoretti *et al.*, Production and detection of cold antihydrogen atoms, Nature (London) **419**, 456 (2002).
[53] G. Gabrielse *et al.*, Background-free observation of cold antihydrogen with field-ionization analysis of its states, Phys. Rev. Lett. **89**, 213401 (2002).